NUMERICAL INVESTIGATION AERODYNAMICS NACELLE-STRAKE EFFECT

J.J. Broekhuijsen[1], G. Vidjaja[2], J.W. van der Burg[2], H.W.M. Hoeijmakers[1]
[1]University of Twente, P.O. Box 217, 7500 AE Enschede, the Netherlands
[2]Airbus Operations GMBH, Airbus-Allee 1, 28199 Bremen, Germany

Keywords: *Nacelle Strake, High-Lift, CFD, Vortex, Boundary-Layer*

Abstract

The focus of this investigation is on the numerical prediction of the nacelle-strake effect on the lift coefficient for transport aircraft in high-lift configurations, i.e. the configurations used in the EUROLIFT II project. Within this project high-Reynolds-number wind-tunnel tests were conducted in the European Transonic Windtunnel (ETW) from 2004 to 2007. The geometry considered, also considered in the present investigation, was a commercial wide-body twin-jet high-lift configuration with flaps and slats in landing configuration. The wind-tunnel model considered is a wing/fuselage configuration with a high bypass ratio through-flow-nacelle with a core body. The complexity of the wind-tunnel model was increased in three successive stages. The final stage III geometry features a nacelle strake on the nacelle inboard surface to optimize the performance of the high-lift configuration.

The applied CFD methods include the usage of hexahedral elements in regions of vortical flow, a RSM-g turbulence model and a version of the dissipation model in terms of Scalar and Matrix dissipation with various coefficients.

Analysis of the results of the performed computations show that for the present configuration, the nacelle strake effect on maximum lift coefficient can be captured with high accuracy by using steady-flow computations and the CFD practices outlined in this paper.

1 Introduction

The three-element high-lift configuration of commercial transport aircraft featuring a slat, a main wing and a Fowler-type of flap is well established. It is an efficient compromise between the lift and the complexity of the mechanical system. The interaction mechanisms between the three elements are understood [1]. However, the geometry of realistic high-lift configurations is more complicated and the interaction phenomena are dominated by vortex flows interaction.

High-lift performance has a major effect on the efficiency, size, economics, take-off and landing performance, fuel consumption, as well as noise emissions, of modern transport aircraft. To satisfy the constantly increasing performance requirements, jet engines are constantly being improved, resulting in larger engine diameters for each new generation of jet engines. Consequently, the engines are very close to the wing, which requires a cut-out of the slat in order to install the engine pylon and nacelle. This slat cut-out leads to aerodynamic interaction phenomena and renders the wing area downstream of the nacelle more sensitive to flow separation, i.e. nacelle wake separation, [2]. To overcome this drawback and to stabilize the flow over the critical wing area, in 1971 Kerker and Wells (McDonnell Douglas) [3] introduced the idea of mounting a pair of strakes on the forward upper part of each nacelle. In landing and take-off configuration the presence of the nacelle strake results in a strong streamwise vortex which travels along the upper side of the wing and interacts with the boundary layer on the upper wing surface and with the vortices from the slat cut-out in such a way that the onset of flow separation on the wing upper surface is delayed. Thus, the nacelle strake vortex recovers a part of the lift loss caused by the installation of the nacelle [4].

It is of considerable interest to capture the nacelle strake effect on the maximum lift coefficient with

CFD [5], [6]. The complex interaction phenomena, in the non-linear range of the lift curve make an accurate prediction of the nacelle strake effect a challenging task. So, the main objective of the present study is to answer the question: can CFD predict the nacelle-strake effect on the lift coefficient?

2 Geometry Wind-Tunnel Model

The baseline geometry (KH3Y) is a commercial wide-body twin-jet high-lift configuration with flaps and slats extended in landing configuration. The wind-tunnel model consists of a wing/fuselage configuration with a high-bypass-ratio through-flow-nacelle with a core body, see Fig. 1a. The difference between the stage II and stage III configurations is a strake mounted at the inboard side of the nacelle. To achieve the objective of the present investigation results from stage II and stage III serve as validation data base. The high-lift configuration has a leading-edge slat and a trailing-edge Fowler flap. The slat is subdivided into three parts, these parts are connected laterally by latches. The slat extends up to the wing tip. The Fowler flap also consists of three parts, the first part extends from the fuselage to the kink in the trailing edge of the wing, and the second part from that point onwards to 71% of the half span. The third element extends from that latter point to the wing tip. The through-flow-nacelle of the KH3Y configuration, which is representative for a modern VHBR-engine with a bypass ratio of about 10, with external mixing, is mounted at 34% half span. The high lift wing is equipped with 487 pressure taps in 10 chordwise sections (DV1 - DV11). Pressure section 3 is not available. Figure 1b shows the top view of the wing including the location of the 10 pressure sections.

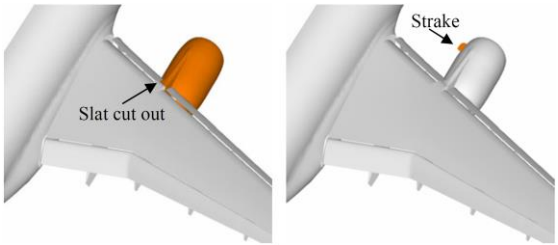

Fig. 1a. Stage II and Stage III KH3Y configuration, [6].

In the EUROLIFT II project a comprehensive test campaign in the European Transonic Windtunnel (ETW) facility in Cologne, Germany has been performed. Conditions were: total temperature 115 K, Mach number M_∞ = 0.2 and Reynolds number Re = 20×10^6, see [7].

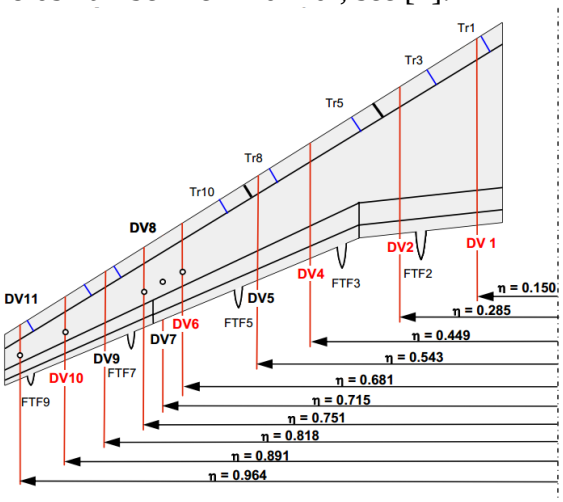

Fig. 1b. Top view of wing high-lift configuration KH3Y, with instrumentation, [8].

3 Numerical Method

Within the present investigation the solver TAU [9] for three-dimensional, compressible, turbulent flow has been employed. TAU utilizes a hybrid unstructured grid, finite-volume-based, multi-grid flow solver suited for parallel computing. In the present study the emphasis is on numerical simulations for steady turbulent flow.

The present investigation uses the SSG/LRR turbulence model with the *g*-equation for providing the length-scale, categorized as the highest level of closure of the Reynolds-averaged Navier-Stokes (RANS) equations for high-Reynolds-number, turbulent flows, see [10], [11], [12].

Since the DLR TAU Code utilizes a central scheme for the discretization of the convective fluxes, artificial dissipation terms are equipped to achieve convergence of the solution procedure.

Description Artificial Dissipation

For a stationary control volume of fixed shape the discretized conservation equations read,

$$\frac{d\boldsymbol{W}}{dt} + \frac{1}{V}\sum_{i=1}^{n}\left(\boldsymbol{Q}_i^{F,c} - \boldsymbol{D}_i\right) = 0 \qquad (1)$$

Here W is the column vector with the conserved variables in a control volume *V* that has *n* bounding faces; $\boldsymbol{Q}_i^{F,c}$ is the column vector of the convective part of the flux through face *i* of the control volume; column vector $\boldsymbol{D}_i$ is the artificial dissipation required for the central scheme used for the convective terms. The scalar form of the artificial dissipation, in a given direction, is expressed as,

$$\boldsymbol{D}_j = d_{j+\frac{1}{2}} - d_{j-\frac{1}{2}} \tag{2a}$$

$$\boldsymbol{d}_{j+\frac{1}{2}} = \alpha_{j+\frac{1}{2}}\left[\varepsilon^{(2)}_{j+\frac{1}{2}}(\boldsymbol{W}_{j+1} - \boldsymbol{W}_{j-1}) - \varepsilon^{(4)}_{j+\frac{1}{2}}(\boldsymbol{W}_{j+2} - 3\boldsymbol{W}_{j+1} + 3\boldsymbol{W}_j - \boldsymbol{W}_{j-1})\right] \tag{2b}$$

i.e. a combination of second-order and fourth-order terms. The factor $\alpha_{j+1/2}$ is the scaling factor that depends on the spectral radius of the Jacobian of the convective flux: $\overline{\overline{J_c}} = \partial \boldsymbol{Q}^{F,c}/\partial \boldsymbol{W}$. The factor in front of the second-order dissipation term equals:

$$\varepsilon^{(2)}_{j+\frac{1}{2}} = \kappa^{(2)}\max(\nu_{j+1}, \nu_j) \tag{2c}$$

The factor in front of the fourth-order dissipation term is:

$$\varepsilon^{(4)}_{j+\frac{1}{2}} = \max(0, \kappa^{(4)} - \varepsilon^{(2)}_{j+\frac{1}{2}}) \tag{2d}$$

Finally, the "pressure sensor" is defined as,

$$\nu_j = \frac{|p_{j+1} - 2p_j + p_{j-1}|}{|p_{j+1} + 2p_j + p_{j-1}|} \tag{2e}$$

It is a measure for pressure gradients in the flow field. In the vicinity of large gradients, like shock waves, ν_j will be large so that $\varepsilon^{(2)}_{j+1/2}$ will be large. Then the fourth-order dissipation term is not required anymore, therefore Eq. (2d) forces $\varepsilon^{(4)}_{j+1/2}$ to reduce to zero. In the present numerical simulations at M_∞ = 0.2, shock waves will not occur (except possibly on the slat in the landing configuration). Therefore the second-order dissipation term is chosen to be zero ($\kappa^{(2)} = 0$) and only the fourth-order dissipation term will be active: $\varepsilon^{(4)}_{j+1/2} = \kappa^{(4)}$. Clearly the fourth-order dissipation factor is uniform in the whole flow field. The fourth-order dissipation term damps high-frequency oscillations and also results in better stability and convergence properties of the scheme [14]. In the scalar artificial-dissipation scheme all dissipative terms are scaled by the same scaling factor, $\alpha_{j+1/2}$, the spectral radius of the Jacobian of the flux term. In upwind schemes the direction in which information is propagated is determined employing the method of characteristics, which allows a representation of (e.g. acoustic) waves without oscillations. So, in order to capture shock waves without oscillations, in the vicinity of shock waves central schemes should mimic the behavior of upwind schemes. The key feature of upwind schemes is that in terms of a central scheme they correspond to a kind of matrix-form of artificial dissipation. Therefore, the motivation for a matrix form of artificial dissipation for a central scheme comes from upwind schemes. The matrix artificial dissipation can be considered as a compromise between scalar and upwind schemes [13].

The matrix form of the artificial dissipation term is obtained by replacing in Eq. (2b) the scalar scaling factor $\alpha_{j+1/2}$ by a matrix derived from the convective flux Jacobian, $\overline{\overline{J_c}} = \partial \boldsymbol{Q}^{F,c}/\partial \boldsymbol{W}$. This matrix contains a scaling of the terms corresponding to the momentum equation, the factor δ. It is used for switching between the matrix and the scalar artificial-dissipation scheme. For $\delta = 1$ the scalar artificial dissipation scheme is utilized, whereas for $\delta = 0$ matrix artificial dissipation is employed. Furthermore, the parameter δ prevents the matrix dissipation from becoming singular at stagnation points where the velocity will be close to zero. For more information reference is made to [9].

The numerical simulations are performed for different settings of the scalar scheme, as well as for the matrix dissipation scheme. In the present study the chosen settings for the artificial dissipation are based on the findings of a separately performed parameter study for the flow about an isolated nacelle with and without a strake, [14]. Based on the results of this parameter study, a CFD best practice has been determined that subsequently has been applied for the numerical simulations of the flow about realistic high-lift configurations.

3.1 Grid

In the present investigation two meshes have been utilized, one for the configuration with strake and one for the configuration without strake. The mesh for the configuration with strake consists of 64,154,180 grid points, while the grid for the configuration without strake contains 66,366,471 grid points. Views of these meshes are presented Figs. 2a-2d. For both configurations 5,211,108 hexahedral elements are used to discretize the space over the upper side of the wing. The hexahedral mesh is surrounded by a layer of pyramids to provide a coupling with the surrounding part of the mesh that consists of tetrahedral elements. Prisms are applied in the boundary layer region, where two directions (along the surface) are resolved isotropic and the third direction is resolved in a nonequidistant fashion. The hexahedral blocks, introduced in the Centaur mesh, are directly attached to the upper surface of the wing in order to adequately resolve the vortical flow induced by the nacelle strake.

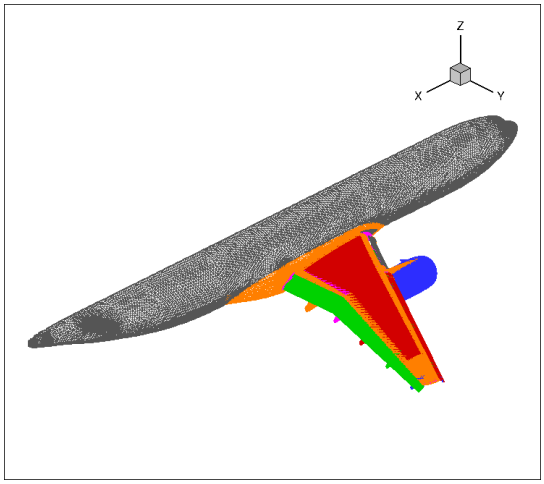

Fig. 2a. Surface mesh of EUROLIFT II model in landing configuration.

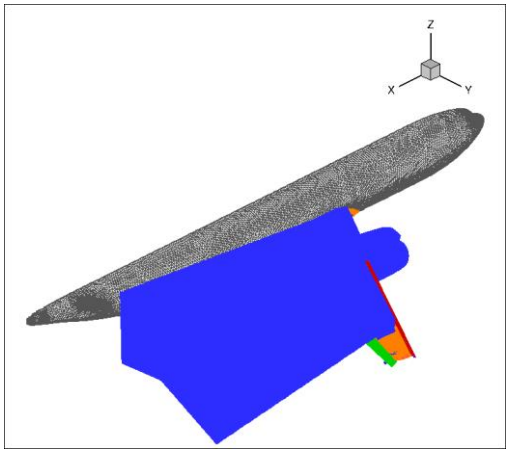

Fig. 2b. Hexahedral blocks attached to upper surface of wing and in wake of wing of EUROLIFT II model in landing configuration.

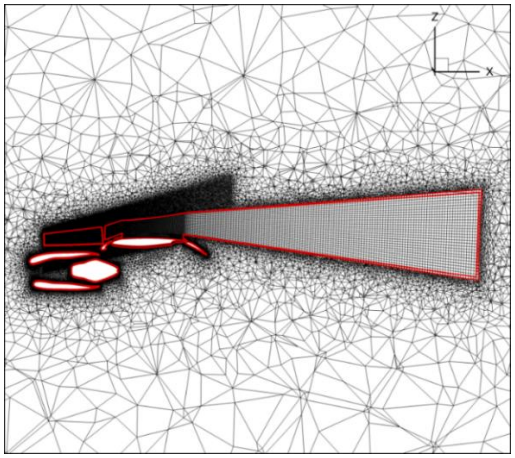

Fig. 2c. Hexahedral and tetrahedral elements in mesh around complex part geometry, intersection at $y/(b/2) = 0.50$.

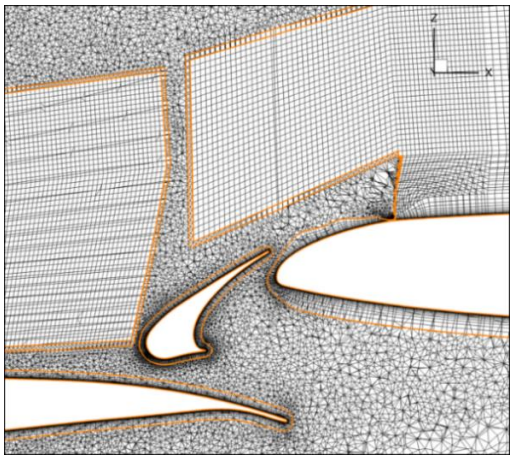

Fig. 2d. Zoom in of mesh with hexahedral and tetrahedral elements around a complex part of geometry, intersection at $y/(b/2) = 0.50$.

4 Prediction Maximum Lift

This section provides a description of the different cases that have been considered. In section 4.1 the settings of the flow solver are given as well as the flow conditions for the computations for steady flow. Also, results of CFD are presented, discussed and interpreted.

4.1 Setting Parameters

In the numerical simulations the amount of artificial dissipation is controlled by selecting the coefficients $\kappa^{(2)}$ and $\kappa^{(4)}$, for the second-order and fourth-order artificial-dissipation terms, respectively, see section 3.
The table below presents the different settings for the calculations performed for the different cases.

Case	S2S	S3S	S2D	S3D
Strake	Off	On	Off	On
Scheme	Scalar dissi.		Scalar dissi.	
$\kappa^{(4)}$	1/64		1/128	
δ	n/a		n/a	

Case	S2P	S3P	S2N	S3N
Strake	Off	On	Off	On
Scheme	Scalar dissi.		Matrix dissi.	
$\kappa^{(4)}$	1/256		1/128	
δ	n/a		0.5	

Table 1. The settings S2S/S3S are used as reference settings. Settings for steady-flow computation are: Turbulence model: RSM-g; Spatial discretization: Central, 4th-order artificial dissipation only; CFL number (fine-grid) CFL = 3; Multi-Grid, number of multigrid levels 1; Number of iterations 30,000; Central convective mean flow flux is average flux.

The initial computation is performed with reference settings of the artificial dissipation, i.e. $\kappa^{(2)} = 0$ and $\kappa^{(4)} = 1/64$ These settings are denoted by S2S (without strake) and S3S (with strake), see Table 1. For the subsequent numerical simulations the artificial dissipation is reduced: first selecting $\kappa^{(4)} = 1/128$ (S2D/S3D) and then $\kappa^{(4)} = 1/256$ (S2P/S3P). Next, a matrix dissipation scheme is applied with the 4th-order dissipation coefficient $\kappa^{(4)} = 1/128$ and a minimum artificial dissipation for velocity of $\delta = 0.5$ (S2N/S3N).
The case with a lower value of δ, i.e. $\delta = 0.2$, did not converge before the maximum lift coefficient was reached. The analysis of this numerical solution suggests that the artificial dissipation is too small to achieve a steady state solution. Therefore these results are not shown here.

For the present investigation a single grid approach with 30,000 iterations for each angle of attack is employed with 1000 start-up iterations with a first-order upwind scheme to initialize the flow field. The CFL number is chosen equal to 3.

4.2 Computational Results

The numerical simulations for steady flow conditions, using the RSM-g turbulence model, have been performed for a Reynolds number of Re = 20×10^6 and a Mach number of $M_\infty = 0.2$.

The flow solution is assessed by analyzing the lift polar, the distribution of the skin friction coefficient and the distribution of the surface pressure coefficient. The vortical flow phenomena in the flow field are studied by means of the distribution of the kinematic vorticity number in combination with the distribution of the velocity component in *x*-direction.
The kinematic vorticity number, often applied in the geological field, see Tikoff and Fossen [15], expresses the ratio of the magnitude of the rate-of-rotation tensor (consisting of the components of the vorticity vector) and the magnitude of the rate-of-strain tensor,

$$W_k = \frac{\left(2R_{ij}R_{ji}\right)^{1/2}}{\left(2S_{ij}S_{ji}\right)^{1/2}} = \frac{|\vec{\omega}|}{\left(2S_{ij}S_{ji}\right)^{1/2}} > 0 \qquad (3)$$

With $\bar{\bar{R}} = \frac{1}{2}(\vec{\nabla}\vec{u} - (\vec{\nabla}\vec{u})^T)$ and $\bar{\bar{S}} = \frac{1}{2}(\vec{\nabla}\vec{u} + (\vec{\nabla}\vec{u})^T)$ the definition of the rate-of-rotation tensor and the rate-of-strain tensor, respectively.
The kinematic vorticity number is always positive. A value larger than unity indicates that the rate of rotation of the local fluid element is exceeds the rate of deformation of the fluid element. This is associated with the flow inside a vortex core.

The behavior of the configuration in the stall regime is considered by investigating the vortical flow structures for angles of attack in the range of $\alpha \in [15°,18°]$, in steps of one degree.
The pressure distribution along the sections, DV1-DV11, see Fig. 1b, are compared with the distributions measured in the ETW wind tunnel.

Convergence history
Figures 3a to 3d present the convergence history of: the residual of the continuity equation (time-rate of change of the density), as well as; that of the lift coefficient for the configuration with and without strake for the different settings of the artificial dissipation listed in Table 1.
Fig. 3a shows the histories of the density residual and lift polar for reference settings (S2S/S3S) (scalar dissipation scheme with $\kappa^{(4)} = 1/64$). After each restart, upon incrementing the angle of attack, the residual drops very rapidly about five orders of magnitude, at least for lower angles of attack. For higher angles of attack unsteady flow phenomena dominate the flow field, resulting in the residual more or less stagnating, though at an acceptable level of 10^{-4}.
Comparing the lift polar for the configuration with and that without nacelle strake, indicates a large difference. The lift coefficient for the case without strake is, while the lift coefficient for the configuration with strake appears to converge to a steady value, substantially above the average value of the configuration without strake.
As can be seen in Fig. 3b, reducing the artificial dissipation to $\kappa^{(4)} = 1/128$, i.e. cases S2D/S3D, the fluctuations in the residual increase in amplitude. Also the rate of convergence decreases slightly compared to that of the cases S2S/S3S, i.e. the ones with reference settings. However, the critical angle of attack is increased by about 1.5°. A similar observation is made for the results for cases S2P/S3P with the still lower artificial dissipation of $\kappa^{(4)} = 1/256$. In that case the density residual reduces approximately to $10^{-3.6}$ orders of magnitude, see Fig. 3c. In this case the difference between the lift polar for the configuration with and that without strake is significantly reduced. A similar observation is made for the results obtained utilizing the matrix dissipation scheme (S2N/S3N), with $\kappa^{(4)} = 1/128$ and $\delta = 0.5$. Fig. 3d shows that the residual drops to about the level $10^{-4.7}$ for the configuration with strake. However, for the configuration without strake the residual drops to a level of $10^{-3.6}$. It should be noted that due to the reduction of the artificial dissipation on the one hand "stronger", more compact, vortices are generated, but on the other hand the numerical procedure becomes less stable. This implies that the solution is entering the regime in which physically unsteady flow phenomena dominate the flow solution.

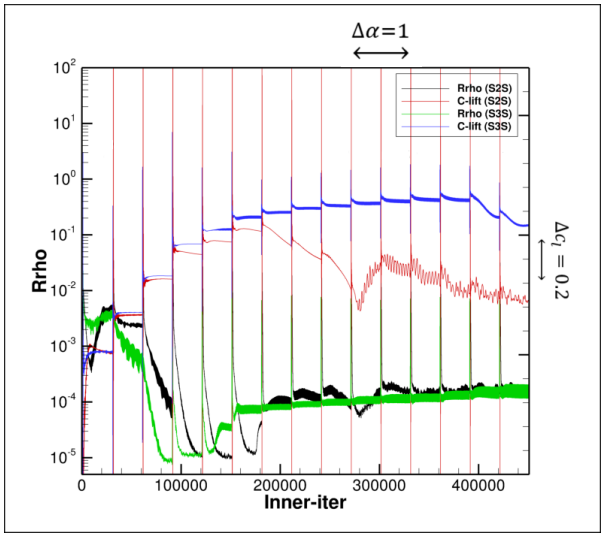

Fig. 3a. S2S/S3S, $\kappa^{(4)} = 1/64$. Convergence history of density residual and history of lift coefficient for sequence of angles of attack.

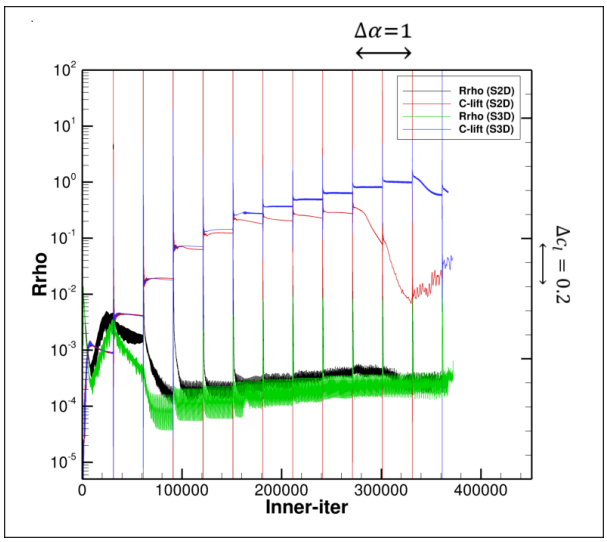

Fig. 3b. S2D/S3D, $\kappa^{(4)} = 1/128$. Convergence history of density residual and history of lift coefficient for sequence of angles of attack.

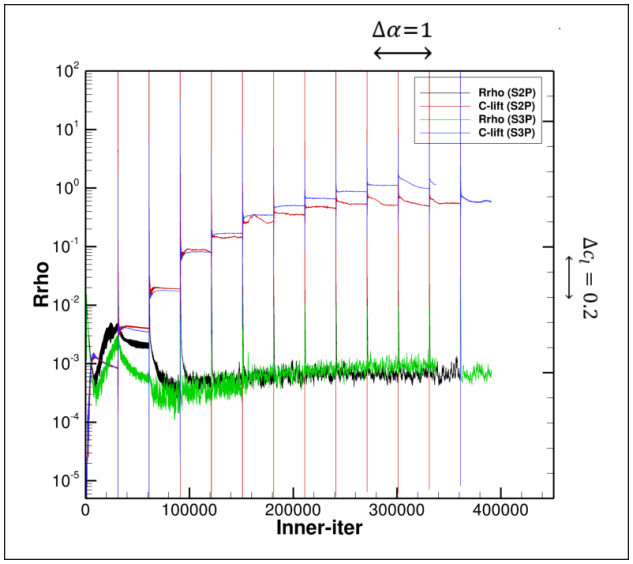

Fig. 3c. S2P/S3P, $\kappa^{(4)}$ = 1/256. Convergence history of density residual and history of lift coefficient for sequence of angles of attack.

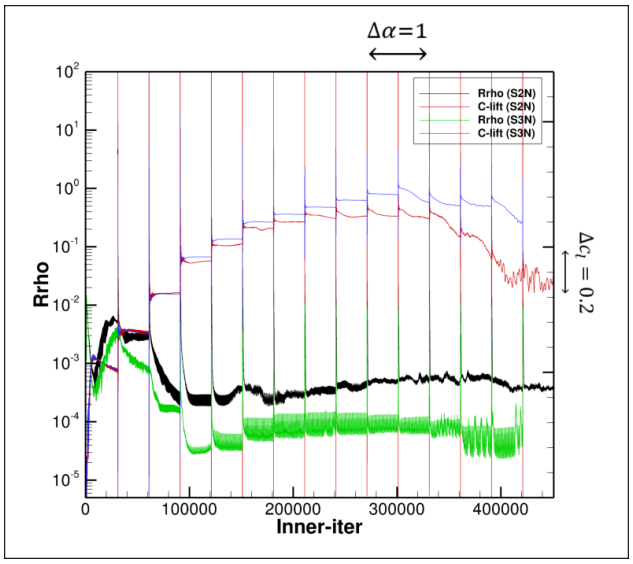

Fig. 3d. S2N/S3N, matrix artificial dissipation with $\kappa^{(4)}$ = 1/128. Convergence history of density residual and history of lift coefficient for sequence of angles of attack.

Lift Polars

The continuous red and blue line in Figs. 4a and 4b correspond to the results from the measurements in the ETW facility for the configuration with and that without strake. Figure 4a presents the computed lift polar for the reference settings $\kappa^{(4)}$ = 1/64, i.e. cases S2S/S3S. It shows that the lift polar is substantially under predicted, already for lower angles of attack. Figure 4b shows that reducing the artificial dissipation to $\kappa^{(4)}$ = 1/128, i.e. cases S2D/S3D, the stall behavior of the configuration without strake improves substantially. Reducing artificial dissipation even further, i.e. cases S2P/S3P to $\kappa^{(4)}$ = 1/256, see figure 4c, shows that in this case the nacelle strake effect can be captured. A nearly identical result is obtained for the matrix dissipation scheme S2N/S3N with $\kappa^{(4)}$ = 1/128 and δ = 0.5. However, a mild under-prediction of maximum lift is observed for cases S2N/S3N compared to the results for cases S2P/S3P. This is caused by the different types of artificial dissipation utilised.

The comparison of the lift polars obtained in the present investigation and the polars obtained in the EUROLIFT II project, H. Frhr. v. Geyr et al. [16] shows a significant improvement in the lift coefficient due to the effect of adding the nacelle strake to the configuration.

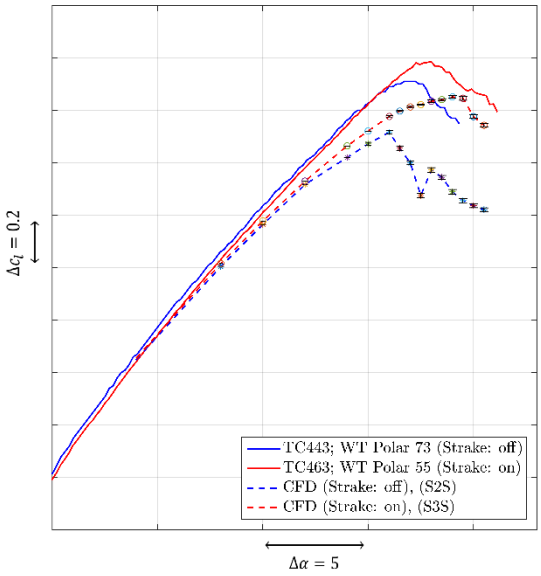

Fig. 4a. Comparison of predicted (S2S/S3S, $\kappa^{(4)}$ = 1/64) and measured lift polars (ETW).
Re = 20×10^6. M_∞ = 0.2.

Wind-tunnel-Installation Effects

The computations for the configurations of the EUROLIFT II project under-predict the lift polar as well as the value of the maximum lift coefficient. Frhr. v. Geyr et al. [16], explained that the measured results have to be corrected for wind-tunnel installation effects before comparing them with results from computations performed assuming free-flight conditions.

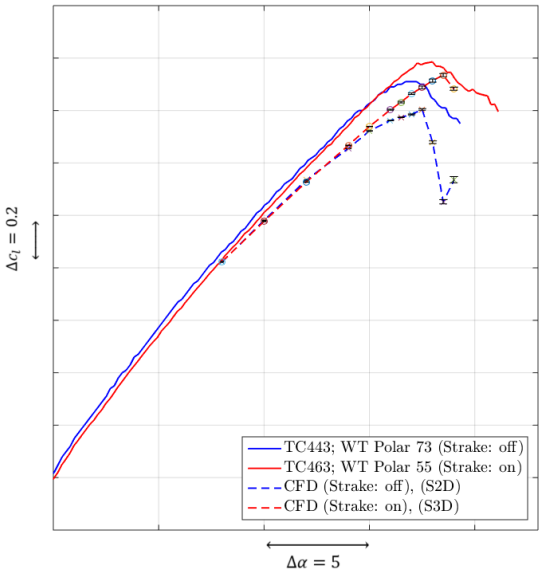

Fig. 4b. Comparison of predicted (S2D/S3D, $\kappa^{(4)}$ = 1/128) and measured lift polars (ETW). Re = 20×10^6. M_∞ = 0.2.

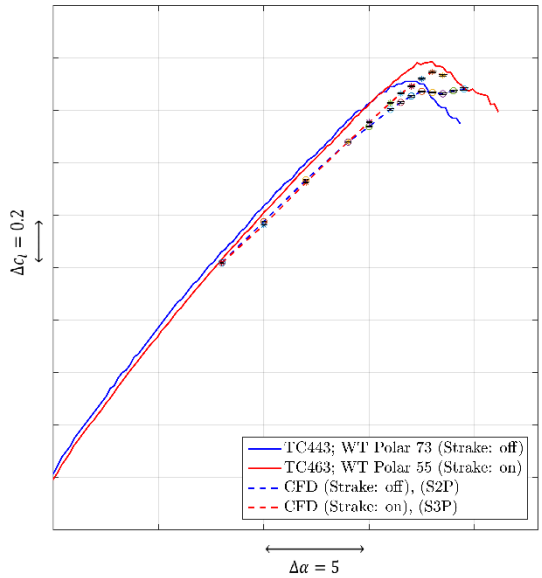

Fig. 4c. Comparison of predicted (S2P/S3P, $\kappa^{(4)}$ = 1/256) and measured lift polars (ETW). Re = 20×10^6. M_∞ = 0.2.

The wind-tunnel model is a so-called half-model. Its plane of symmetry coincides with one of the walls of the wind tunnel. The installation effects increase the inboard loading of the wing of the half-model due to cross-flow components of the flow. In the numerical simulation the wind-tunnel walls are treated as slip walls. Therefore, the

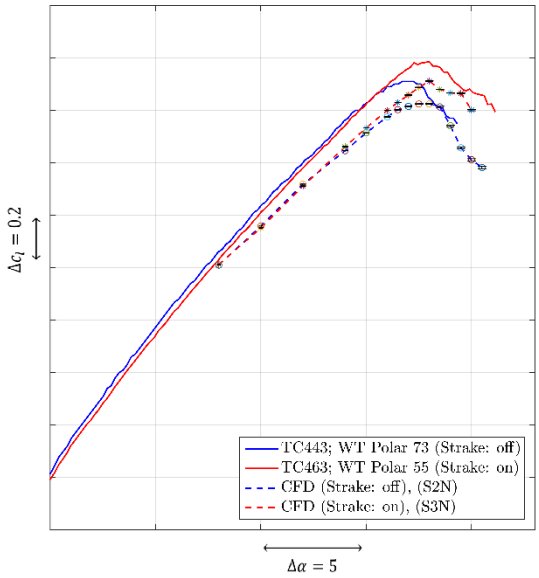

Fig. 4d. Comparison of predicted (S2N/S3N, $\kappa^{(4)}$ = 1/128, δ = 0.5) and measured lift polars (ETW). Re = 20×10^6. M_∞ = 0.2.

suction peaks in the computed pressure distribution in the root section (DV1) are under-predicted. This can be seen in the pressure distributions of the present investigation, see Fig. 8a. According to Rudnik et al. [8], the under-prediction of the lift coefficient is to be expected comparing numerical results for free-flight conditions with corrected wind tunnel measurements. This behavior is also identified in the predicted lift polars of the present investigation. Seen in this light, the agreement of the numerical solutions and measurements are regarded as accurate.

A comparison of the predicted lift polars for different settings for artificial dissipation shows that there is a strong effect of artificial dissipation on the computed lift coefficient. This also suggests a strong grid dependency. A lower artificial dissipation results in a stronger and a more compact vortex system originating from the edges of the slat cut-out and the nacelle pylon. This successfully delays, especially for the configuration without strake, the onset of flow separation

4.3 Prediction Stall Mechanisms

4.3.1 Distribution skin friction coefficient

For lower angles of attack, typically around 15°, the flow is attached to the main wing for each setting used for the artificial dissipation. However, reducing artificial dissipation, which intensifies the vorticity field, results in small regions with separated flow to the left of the flap tracks, see Fig. 5a (left).

For the cases S2S/S3S, $\kappa^{(4)} = 1/64$, increasing the angle of attack from $\alpha = 16°$ to $\alpha = 17°$, shows that the flow starts to separate on the upper surface of the main wing near the trailing edge for the configuration without strake (S2S). In the computations with lower artificial dissipation the flow stays attached. The computation for $\alpha = 18°$ shows a large region with separated flow in the critical area of the wing, indicating nacelle wake separation, see Figure 5b (left), for the configuration without strake (S2S, $\kappa^{(4)} = 1/64$), as well as a region with starting separated flow for lower artificial dissipation (S2D, $\kappa^{(4)} = 1/128$). As is observed in Fig. 5c for the configuration without strake (S2P, $\kappa^{(4)} = 1/256$) at $\alpha = 18°$, the skin friction lines recirculate at the inner slat in the region close to the pylon. With the occurrence of this slat separation on the main wing, flow separation develops upstream of the trailing edge. The effect of flow separation is not observed for the configuration with strake, Fig. 5c (S3P $\kappa^{(4)} = 1/256$), this is possibly due to the nacelle strake vortex re-energizing the boundary-layer flow in this region. The flow separation clearly depends on the level of artificial dissipation, i.e. flow remains attached longer for lower artificial dissipation.

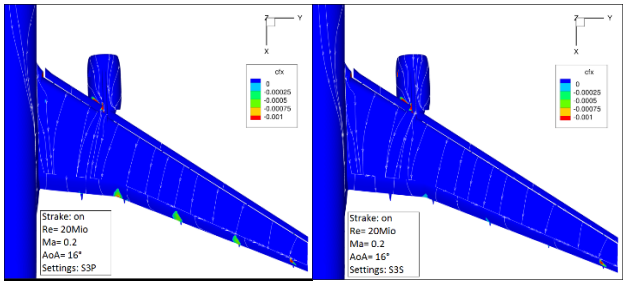

Fig. 5a. Configuration with strake at $\alpha = 16°$. Skin-friction lines and distribution of x-component skin friction coefficient (c_{fx}) for case S3S ($\kappa^{(4)} = 1/64$) (right) and S3P ($\kappa^{(4)} = 1/256$) (left). Re = 20×10^6, $M_\infty = 0.2$.

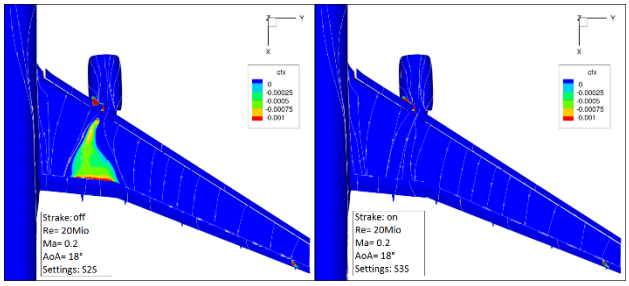

Fig. 5b. Configuration with strake (S3S, right) and without strake (S2S, left), at $\alpha = 18°$. Skin-friction lines and distribution x-component skin friction coefficient (c_{fx}) Artificial dissipation S2S/S3S is $\kappa^{(4)} = 1/64$. Re = 20×10^6, $M_\infty = 0.2$.

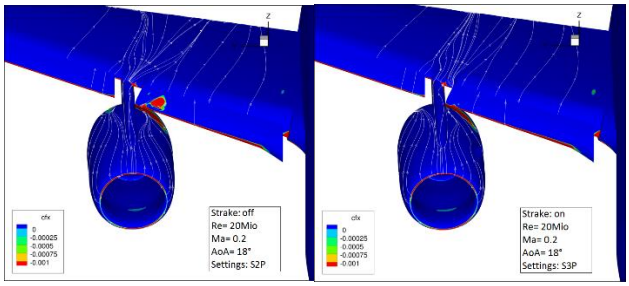

Fig. 5c. Configuration, with strake (S3P, right) and without strake (S2P, left), at $\alpha = 18°$. Skin-friction lines and distribution x-component skin friction coefficient (c_{fx}) for case S2P/S3P is $\kappa^{(4)} = 1/256$. Re = 20×10^6, $M_\infty = 0.2$.

4.3.2 Flow field

The flow field is analyzed employing iso-surfaces of the kinematic vorticity number W_k, defined in section 4.2. It is a measure of the amount of rotation relative to the amount of deformation of fluid elements. In this paper we employ iso-surfaces with a fixed value of $W_k = 1.3$. The effect of reducing artificial dissipation is investigated by visualizing the kinematic vorticity number as well as the streamwise velocity on cross-flow planes cutting through the hexahedral mesh.

Distribution kinematic vorticity number

The effect of the different levels of artificial dissipation can clearly be observed in the distribution of the kinematic vorticity number. To distinguish between the directions of rotation, the blue iso-surfaces indicate counter-clockwise rotation, when looking in the same direction as the free stream. As shown in Fig. 6a, the nacelle

strake vortex and its trajectory are clearly visualized and resolved. When comparing results obtained for different levels of artificial dissipation, it is observed that the vortex generated by the nacelle breaks down for the cases with reduced artificial dissipation. The resulting wake interacts with the nacelle strake vortex, as can be seen in Fig. 6a (α = 18°). Examining the vortex system of the configuration without strake in Fig. 6b more closely, shows that the vortices created by the slat cut-out are better represented and stronger for lower levels of the artificial dissipation. This appears to improve the stall behavior of this configuration. This then allows the line of thought that an adequate resolution of the vortices in this region is of importance for an accurate prediction of the maximum lift coefficient.
Moreover, considering the nacelle strake vortex for different settings of artificial dissipation, a roll-up of the nacelle strake vortex can be identified, see Fig. 6a. This phenomenon is related to vortex breakdown, see van Jindelt [17], [18].

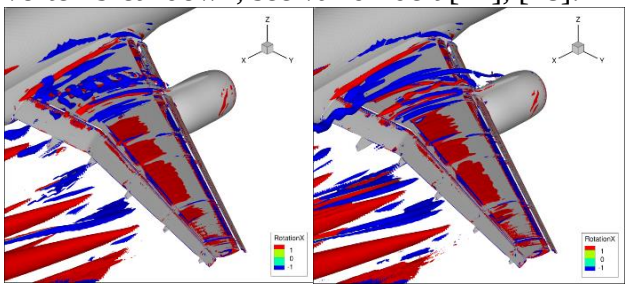

Fig. 6a. Iso-surface of kinematic vorticity number W_k = 1.3 for configuration at α = 18° without (S2P, left) and with (S3P, right) nacelle strake. Artificial dissipation settings S2P/S3P is $\kappa^{(4)}$ = 1/256. Re = 20×10^6, M$_\infty$ = 0.2.

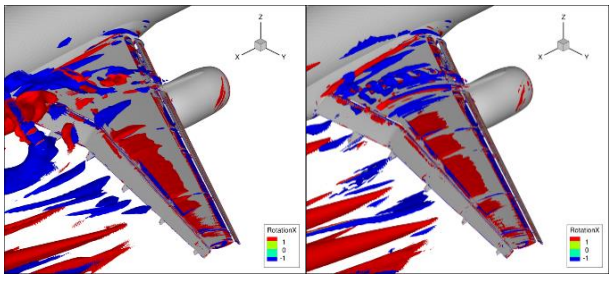

Fig. 6b. Iso-surface of kinematic vorticity number W_k = 1.3 for configuration at α = 18° without nacelle strake for different artificial dissipation settings: left S2S ($\kappa^{(4)}$ = 1/64); right: S2P ($\kappa^{(4)}$ = 1/256). Re = 20×10^6, M$_\infty$ = 0.2.

Analysis of the distribution of the kinematic vorticity number W_k in cross-flow planes supports the observations made so far. This is clearly seen in Fig. 6c and 6d, in which the vortical structures become more concentrated when reducing artificial dissipation. This effect and the related effect on flow separation, i.e. reducing artificial dissipation, results in a stronger, compacter, vortical system. In numerical simulations this defines a key factor in capturing the nacelle-strake effect.

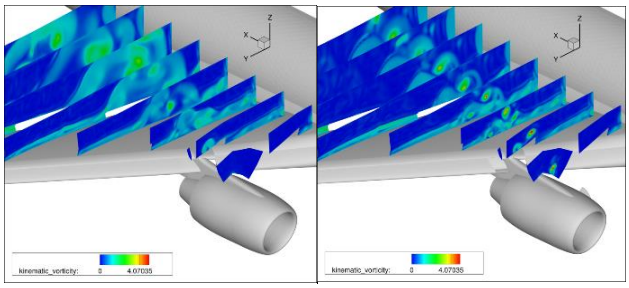

Fig. 6c. Distribution of kinematic vorticity number W_k in cross-flow planes for configuration without (S2S, left) and with (S3S, right) nacelle strake. S2S/S3S artificial dissipation settings: $\kappa^{(4)}$ = 1/64. Re = 20×10^6, M$_\infty$ = 0.2.

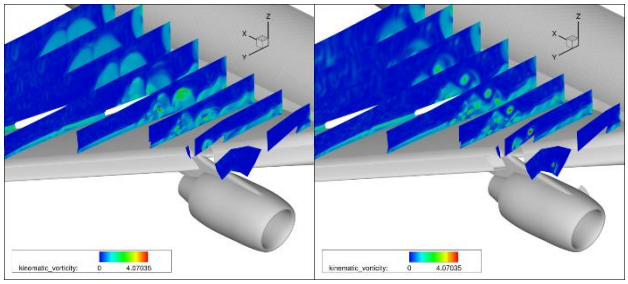

Fig. 6d. Distribution of kinematic vorticity number W_k in cross-flow planes for configuration without (S2P, left) and with (S3P, right) nacelle strake. S2P/S3P artificial dissipation settings: $\kappa^{(4)}$ = 1/256. Re = 20×10^6, M$_\infty$ = 0.2.

Distribution x-component velocity

Figures 7a and 7b show the distribution of the *x*-component of the velocity in selected successive cross-flow planes. For the configuration without strake, already for an angle of attack of 15°, there is a region with low velocity above the slat (slat separation) for all settings of the artificial dissipation, see Fig. 7a. This region develops into a region with separated flow on the main wing.

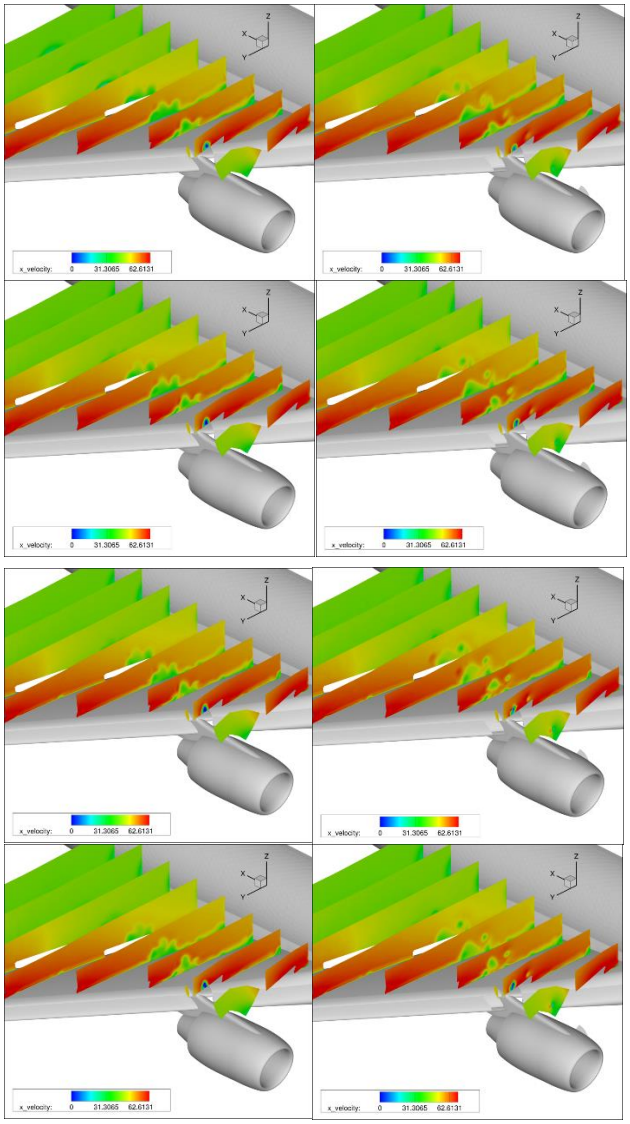

Fig. 7a: Distribution of *x*-component of velocity in sequence of cross-flow planes for configuration without (left) and with (right) nacelle strake. From top to bottom: S2S/S3S($\kappa^{(4)}$ = 1/64), S2D/S3D ($\kappa^{(4)}$ = 1/128), S2P/S3P($\kappa^{(4)}$ = 1/256), S2N/S3N ($\kappa^{(4)}$ = 1/128, δ = 0.5).
Re = 20×10^6, M_∞ = 0.2, α = 15°.

This behavior is consistent with the observations made in the wind tunnel for the surface flow on the wing.
With increasing angle of attack, see Fig. 7b, and for high artificial dissipation, a large area with separated flow develops above the wing for the configuration without strake. This region with separated flow is successfully suppressed by the vortex from the nacelle strake.

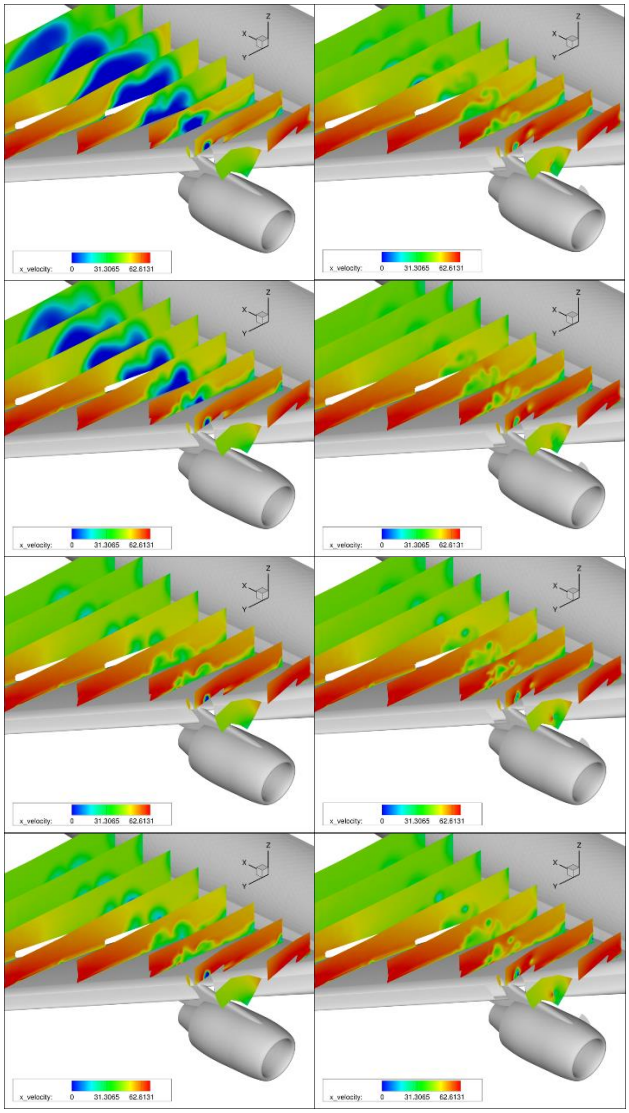

Fig. 7b: Distribution of *x*-component of velocity in sequence of cross-flow planes for configuration without (left) and with (right) nacelle strake. From top to bottom: S2S/S3S($\kappa^{(4)}$ = 1/64), S2D/S3D($\kappa^{(4)}$ = 1/128), S2P/S3P($\kappa^{(4)}$ = 1/256), S2N/S3N($\kappa^{(4)}$ = 1/128, δ = 0.5).
Re = 20×10^6, M_∞ = 0.2, α = 18°.

Fig. 7a indicates very clearly the effect of lowering artificial dissipation on the flow field in terms of the *x*-component of the velocity: the effect of the reduced artificial dissipation has a larger impact on the configuration without strake than on the configuration with strake. This is due to the effect of the strong and dominating nacelle-strake vortex.
For the configuration without strake the critical region of the flow is affected by vortices from different origin and their interaction phenomena.

Therefore, for this configuration, the numerical simulation of the flow is a very delicate matter. For this case the vortices, resulting from the slat cut-out and from the nacelle, should be accurately resolved in the mesh.
So, in order to obtain a better representation of the physics in the results of the computations a refinement of the grid in the critical flow region of the computational domain is highly recommended.

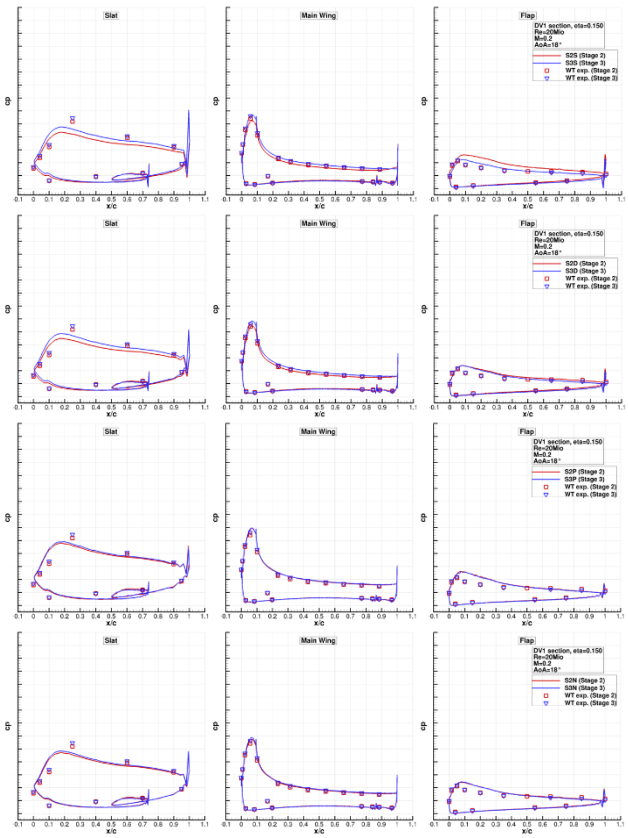

Fig. 8a. Predicted and measured (ETW) chord wise pressure distributions section DV1 ($y/(b/2)$ = 0.15) for configuration without (stage 2) and configuration with (stage 3) nacelle strake.
From top to bottom: S2S/S3S($\kappa^{(4)}$ = 1/64), S2D/S3D($\kappa^{(4)}$ = 1/128), S2P/S3P($\kappa^{(4)}$ = 1/256), S2N/S3N($\kappa^{(4)}$ = 1/128, δ = 0.5).
Re = 20×10^6, M_∞ = 0.2, α = 18°.

4.3.4 Chord-wise pressure distribution comparison with measurements in ETW

The surface pressure distribution is presented separately for the slat, the main wing and the flap. The local chord of the individual elements is used to non-dimensionalize the chord wise coordinate. The pressure distributions use the same origin of the individual elements which allows a direct comparison of the graphs.
Generally, the predicted and measured data agree quite well. However, note that the wind-tunnel installation effects increase the inboard loading of the wing. This is due to induced cross-flow (spanwise) velocity components related to using a half-model in the wind tunnel.

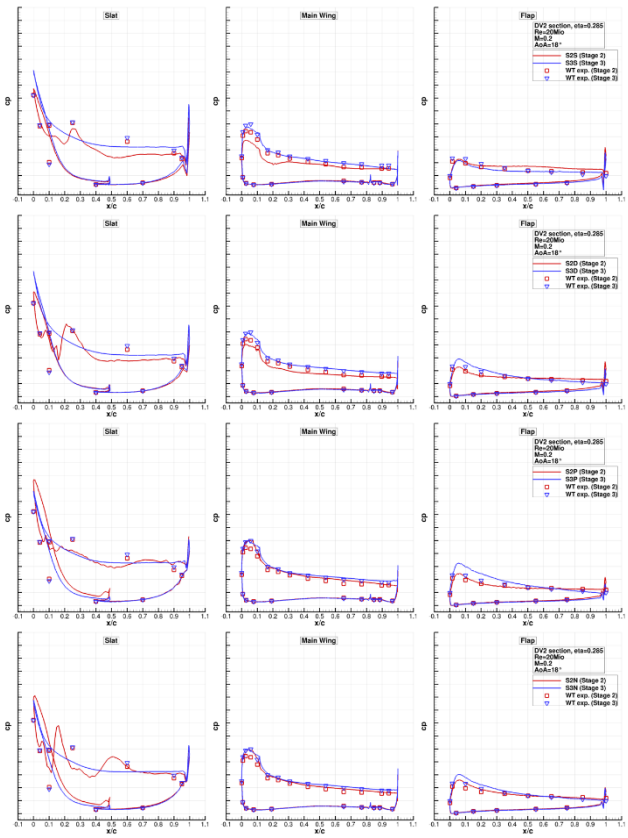

Fig. 8b. Predicted and measured (ETW) chord wise pressure distributions section DV2 ($y/(b/2)$ = 0.285) for configuration without (stage 2) and configuration with (stage 3) nacelle strake.
From top to bottom: S2S/S3S($\kappa^{(4)}$ = 1/64), S2D/S3D($\kappa^{(4)}$ = 1/128), S2P/S3P($\kappa^{(4)}$ = 1/256), S2N/S3N($\kappa^{(4)}$ = 1/128, δ = 0.5).
Re = 20×10^6, M_∞ = 0.2, α = 18°.

This results in general in an under-prediction of the suction peaks, especially for the first pressure section (DV1, $y/(b/2)$ = 0.15), see Fig. 7a. This is also the explanation for the under-prediction of the lift curves. Fig. 7b shows for a high value of the artificial dissipation (S2S/S3S), as well as for

lower levels of the artificial dissipation (S2D/S3D) that the flow over the slat has a strong tendency to separate. The pressure distribution along the second section (DV2, $y/(b/2) = 0.285$) together with the skin friction lines, Fig. 5c, indicate that flow separation on the main wing is induced by the flow separation on the slat.
The latter is evident from the strong reduction in the leading-edge suction peak in the pressure distribution on the main wing. The flow separation on the slat and the associated loss in total pressure in its wake causes separation of the flow on the upper surface of the main wing in the region downstream of the slat. The suction peak of the flap is less affected. So, the observed lift breakdown is consistent with the interaction of the nacelle vortex and the flow over the wing as sketched above. For cases S2S/S3S and S2D/S3D the flow separation evident in the pressure distribution along the second section (DV2) is strongly developed for the slat and the main wing, see Fig. 8b. A similar but weaker effect can be seen for the first and fourth pressure section for the different levels of artificial dissipation, also for an angle of attack of 19°. As follows from the measurements and from the results of the numerical simulations, the vortex from the nacelle strake successfully delays the onset of flow separation along the second pressure section to a higher angle of attack.

5. Concluding Remarks

The most outstanding and important result of the performed computational study is that for the current configuration the effect of the nacelle strake on maximum lift coefficient can be captured with high accuracy, employing steady flow simulations and the CFD practices defined in section 4.1. The effects on the numerical solution due to variation of the artificial dissipation shows that the scalar dissipation scheme with a 4^{th}-order dissipation factor of 1/256 is the least dissipative scheme. This scheme results in the most accurate prediction of the effect of the nacelle strake on the lift polar. However, the artificial dissipation with matrix dissipation leads also to a quite accurate solution. This allows the conclusion that the effect of the nacelle strake on the maximum lift coefficient is mainly dominated by complex vortical flow structures and their interaction with the boundary layer on the wing upper surface downstream of the nacelle. PIV measurements performed in the low-speed wind tunnel of Airbus-Deutschland in Bremen [18] confirm this. So, to numerically predict the effect of the nacelle strake requires an accurate representation of the vortices from the nacelle. In addition, the validation of the results of the CFD computations based on the ETW measurements shows consistency regarding the effect of the nacelle strake on stall behavior of the configuration.

However, the maximum lift coefficient is slightly under predicted for the configuration without as well as for the configuration with nacelle strake, irrespective of the coefficients of the artificial dissipation. This finding is related to wind-tunnel-installation effects. These installation effects of the half-model cause an increase in the inboard loading of the wing due to induced cross-flow velocity components.
In the present investigation numerical simulations have been carried out employing the version of TAU solving the Unsteady-Reynolds-averaged Navier-Stokes equations (URANS). For these time-accurate numerical simulations the artificial dissipation settings of cases S2P/S3P and S2N/S3N have been used. The results shows consistency with the results from numerical simulations assuming the flow to be steady. This implies that the physics behind the effect of the nacelle strake on the flow can be captured using the employed CFD practices.

Comparison of results of PIV measurements at low speed ($Re = 1.4\times10^6$) for the case without and the case with strake [18] shows that the upwash, i.e. induced velocity by the inboard nacelle vortex, results in earlier flow separation on the main wing. The effect of the nacelle strake vortex is to reduce or eliminate the detrimental effects of the nacelle vortices by feeding high kinetic energy air into the critical region of the surface flow. Moreover, the trajectory of the nacelle-strake vortex obtained in the numerical simulations matches the trajectory that is extracted from the PIV measurements very well. This suggests that the effect of Reynolds number on the trajectory of the nacelle-strake vortex is weak.

6. Recommendations

For further investigation of the nacelle-strake effect it is highly recommended to improve the mesh in the regions featuring vortical flow and in regions in which interaction of vortices with the boundary layer. The present investigation shows that the resolution in the region dominated by vortical flow has to be improved by grid refinement.
Specifically around the slat cut-out the vortical flow generated there plays a major role in the stall behavior of a high-lift configuration. One way of improving the accuracy in this region is to refine the unstructured mesh or replace it by an embedded structured mesh.
Furthermore, it is recommended to perform calculations using a smaller increment $\Delta\alpha$ in angle of attack in order to obtain higher resolution of the lift polar. Another but related approach is to conduct so-called intermediate stages between the different main stages, for example, if 30,000 iterations have been performed for α = 18°, before performing 30,000 iterations for α = 18.5°, for example 3000 iterations are performed for 18.1°, 18.2°, 18.3° and 18.4°.
The current investigation shows that the effect of the nacelle strake on maximum lift coefficient can be captured with CFD with high accuracy. A next step could be to carry out a detailed study on different convergence acceleration methods.

In the present investigation the vortices are visualized utilizing the kinematic vorticity number W_k. A problem associated with this variable is that it cannot distinguish between swirling motions and shearing motions in a flow field Another approach is based on the triple decomposition of the velocity gradient tensor. The idea behind this approach is to extract the so-called pure swirling motion. The aim is to decompose an arbitrary instantaneous state of the relative motion into three elementary motions; pure shearing (elongation), rigid body rotation and irrotational straining (shearing). In this case the elongation tensor should be symmetric, the rigid-body-rotation tensor antisymmetric and the shearing-tensor purely asymmetric. The method has been applied to planar flows, its effectiveness for identification of three-dimensional vortical structures, however, is not clear, Kolár [20].
Finally, since the nacelle-strake effect can be predicted, which is also shown for other test cases, an optimization study on the installation point and shape of the nacelle strake (e.g. using a POD approach) might be pursued.

References

[1] Smith, A.M.O. High-Lift Aerodynamics, 37th Wright Brothers Lecture, AIAA Paper No. 74-939, AIAA 6th Aircraft Design, Flight Test and Operations Meeting, Los Angeles, CA, August 12-14, 1974.

[2] van Dam, C. The aerodynamic design of multi-element high-lift systems for transport airplanes. Progress in Aerospace Sciences, vol. 38, no. 2, pp. 101–144, 2002.

[3] Kerker, R. and Wells, O. *Liftvanes*. US Patent 3,744,745, July 10, 1973.

[4] Gad-el Hak, M., Pollard, A. and Bonnet, J.-P. *Flow control: Fundamentals and practices*. Vol. 53. Springer Science & Business Media, 2003.

[5] Haines, A.B. *Scale effects on aircraft and weapon aerodynamics.* AGARDograph 323, DTIC Document ADA291964, 1994.

[6] Rudnik, R. Stall behaviour of the EUROLIFT high lift configurations. *46th AIAA Aerospace Sciences Meeting and Exhibit,* AIAA Paper 2008-836, 2008.

[7] Rudnik, R. *Final Publishable REPORT*. AST3-CT04-502896, 2007

[8] Rudnik, R. and von Geyr, H. The European high lift project EUROLIFT II - Objectives, approach, and structure. *25th AIAA Applied Aerodynamics Conference*, AIAA Paper 2007-4296, 2007.

[9] DLR. *Technical documentation of the DLR TAU Code Release* 2016.10. Deutsches Zentrum für Luft- und Raumfahrt e.V., Technical Report, 2016.

[10] Pope, S.B. *Turbulent Flow*. Cambridge University Press, 1st ed., 2000.

[11] Togiti, V. and Eisfeld, B. Assessment of g-equation formulation for a second-moment Reynolds stress turbulence model. *22nd AIAA Computational Fluid Dynamics Conference*, AIAA Paper 2015-2925, 2015.

[12] Eisfeld, B. Reynolds stress modelling for complex aerodynamic flows. 5th *European Conference on Computational Fluid Dynamics, ECCOMAS CFD*, pp. 14–17, 2010.

[13] Swanson, R.C., Radespiel, R. and Turkel, E. On some numerical dissipation schemes. *Journal of Computational Physics*, Volume 147, Issue 2, 1998, pp. 518-544.

[14] Broekhuijsen, J.J. *Numerical investigation of nacelle strake effect*. MSc Thesis, University of Twente, Enschede, the Netherlands, 2017.

[15] Tikoff, B. and Fossen, H. The limitations of three-dimensional kinematic vorticity analysis. *Journal of Structural Geology*, Vol. 17, No. 12, pp. 1771–1784, 1995.

[16] Frhr. von Geyr, H., Schade, N., van der Burg, J.W., Eliasson, P. and Esquieu, S. CFD-prediction of maximum-lift-effects on realistic high-lift-commercial-aircraft-configurations within the European project EUROLIFT II. *25th AIAA Applied Aerodynamics Conference*, AIAA Paper 2007-4299, 2007.

[17] van Jindelt. T. *Numerical investigation of vortex breakdown.* MSc thesis, University of Twente, the Netherlands, 2015.

[18] van Jindelt, T., van der Burg, J.W., van der Weide, E.T.A. and Hoeijmakers, H.W.M. Numerical investigation of vortex breakdown. 34th AIAA Applied Aerodynamics Conference, AVIATION Forum 2016, Washington D.C. June 13 – 17, 2016. AIAA Paper 2016-4174, 2016.

[19] Quix, H., Schulz, M., Quest, J., Rudnik, R. and Schröder, A. Low speed high lift validation tests within the European project EUROLIFT II. *25th AIAA Applied Aerodynamics Conference*, AIAA Paper 2007-4298, 2007.

[20] Kolár, V. Vortex identification: New requirements and limitations. *International Journal of Heat and Fluid Flow*, vol. 28, no. 4, pp. 638–652, 2007.

Copyright Statement